

all of the H- and L-chain mutations required for bnAb activity against the native CD4bs. Indeed, no neutralizing activity was detected for any of the 8 eOD-GT8 60mer-induced Abs [all with high affinity ($K_D < 1 \text{ nM}$) for eOD-GT8 and low affinity ($1 \mu\text{M} < K_D < 100 \mu\text{M}$) for core-e-2CC HxB2 N276D] that we tested against a panel of four viruses from clades A and B that included both WT and N276A mutant viruses with increased sensitivity to VRC01-class bnAbs (fig. S18). One design feature of eOD-GT8 is that it lacks the N276 glycan; removal of this glycan is a requirement for germline reactivity (17, 21). However, the N276 glycosylation site is conserved in 94.5% of HIV strains, according to an analysis of 3796 sequences from the Los Alamos HIV database (www.hiv.lanl.gov/). Induction of broad neutralization will probably require one or more boosting immunogens bearing a glycan at N276 so as to select mutations to accommodate that glycan (17). On the H chain of VRC01-class bnAbs, mutations in the CDR2, CDRI, FW1, and FW3 are likely required for maximum potency and breadth (24, 40), and native-like Env immunogens will probably be needed to select for these. In sum, boosting with a sequence of increasingly native-like antigens, and potentially including cocktails of different antigens within each boost to mimic the antigenic diversity of the CD4bs, will likely be needed to select the mutations required for VRC01-class bnAb activity. The mouse model presented here, as well as other newly developed VRC01-class knock-in mouse models (41), should aid us to test this notion and can be used to identify the antigens and boosting strategies that work best. Of note, we demonstrated here that a single immunization with the eOD-GT8 60mer induces VRC01-class antibodies with modest affinity for the core-e-2CC HxB2 N276D monomer and 60mer, so these molecules represent promising candidates for the first boost. We are thus mapping the first steps in a sequential strategy for the rational induction of bnAbs against HIV.

REFERENCES AND NOTES

- H. X. Liao et al., *Nature* **496**, 469–476 (2013).
- N. A. Doria-Rose et al., *Nature* **509**, 55–62 (2014).
- M. C. Gaudin et al., *Nat. Med.* **3**, 1389–1393 (1997).
- J. R. Mascola et al., *Nat. Med.* **6**, 207–210 (2000).
- P. W. Parren et al., *J. Virol.* **75**, 8340–8347 (2001).
- B. Moldt et al., *Proc. Natl. Acad. Sci. U.S.A.* **109**, 18921–18925 (2012).
- J. Pietsch et al., *Proc. Natl. Acad. Sci. U.S.A.* **109**, 15859–15864 (2012).
- M. Shingai et al., *J. Exp. Med.* **211**, 2061–2074 (2014).
- X. Wu et al., *Science* **329**, 856–861 (2010).
- T. Zhou et al., *Science* **329**, 811–817 (2010).
- X. Wu et al., *Science* **333**, 1593–1602 (2011).
- J. F. Scheid et al., *Science* **333**, 1633–1637 (2011).
- M. Bonsignori et al., *J. Virol.* **86**, 4688–4692 (2012).
- T. Zhou et al., *Immunity* **39**, 245–258 (2013).
- I. S. Georgiev et al., *Science* **340**, 751–756 (2013).
- A. P. West Jr., R. Diskin, M. C. Nussenzweig, P. J. Bjorkman, *Proc. Natl. Acad. Sci. U.S.A.* **109**, E2083–E2090 (2012).
- J. Jardine et al., *Science* **340**, 711–716 (2013).
- R. Arnaut et al., *PLOS ONE* **6**, e22365 (2011).
- B. J. DeKosky et al., *Nat. Med.* **21**, 86–91 (2015).
- S. Hoot et al., *PLOS Pathog.* **9**, e1003106 (2013).

- A. T. McGuire et al., *J. Exp. Med.* **210**, 655–663 (2013).
- X. Xiao et al., *Biochem. Biophys. Res. Commun.* **390**, 404–409 (2009).
- Single-letter abbreviations for the amino acid residues are as follows: A: Ala; C: Cys; D: Asp; E: Glu; F: Phe; G: Gly; H: His; I: Ile; K: Lys; L: Leu; M: Met; N: Asn; P: Pro; Q: Gln; R: Arg; S: Ser; T: Thr; V: Val; W: Trp; and Y: Tyr.
- J. R. Mascola, B. F. Haynes, *Immunol. Rev.* **254**, 225–244 (2013).
- I. S. Georgiev et al., *J. Immunol.* **192**, 1100–1106 (2014).
- D. Sok et al., *PLOS Pathog.* **9**, e1003754 (2013).
- X. Xiao, W. Chen, Y. Feng, D. S. Dimitrov, *Viruses* **1**, 802–817 (2009).
- D. S. Dimitrov, *mAbs* **2**, 347–356 (2010).
- B. F. Haynes, G. Kelsoe, S. C. Harrison, T. B. Kepler, *Nat. Biotechnol.* **30**, 423–433 (2012).
- F. Klein et al., *Science* **341**, 1199–1204 (2013).
- X. Wu et al., *Cell* **161**, 470–485 (2015).
- M. M. Souto-Carneiro, N. S. Longo, D. E. Russ, H. W. Sun, P. E. Lipsky, *J. Immunol.* **172**, 6790–6802 (2004).
- A. B. Morelli et al., *J. Med. Microbiol.* **61**, 935–943 (2012).
- R. W. Sanders et al., *PLOS Pathog.* **9**, e1003618 (2013).
- J. P. Julian et al., *Science* **342**, 1477–1483 (2013).
- D. Lyumkis et al., *Science* **342**, 1484–1490 (2013).
- M. Pancera et al., *Nature* **514**, 455–461 (2014).
- B. Dey et al., *PLOS Pathog.* **5**, e1000445 (2009).
- R. Diskin et al., *Science* **334**, 1289–1293 (2011).

- F. Klein et al., *Cell* **153**, 126–138 (2013).
- P. Dosenovic et al., *Cell* **161**, 1505–1515 (2015).

ACKNOWLEDGMENTS

We thank T. R. Blane, S. Kupriyanov, and G. S. Martin for technical assistance. The data presented in this manuscript are tabulated in the main paper and in the supplementary materials. This work was supported by the IAVI Neutralizing Antibody Consortium and Center (W.R.S. and D.R.B.); the Collaboration for AIDS Vaccine Discovery funding for the IAVI NAC (W.R.S. and D.R.B.); the Ragon Institute of MGH, MIT and Harvard (D.R.B. and W.R.S.); the Helen Hay Whitney Foundation (J.G.J.); and National Institute of Allergy and Infectious Diseases grants R01-AI073148 (D.N.), P01-AI081625 (W.R.S.), and CHAVI-ID 1UM1AI100663 (W.R.S. and D.R.B.). IAVI and the Scripps Research Institute are filing a patent relating to the eOD-GT8 immunogens in this manuscript, with inventors J.G.J., D.W.K., S.M., and W.R.S. Materials and information will be provided under a material transfer agreement.

SUPPLEMENTARY MATERIALS

www.sciencemag.org/content/349/6244/156/suppl/DC1
Materials and Methods
Figs. S1 to S18
Tables S1 to S8
References (42–53)

16 May 2015; accepted 11 June 2015
Published online 18 June 2015;
10.1126/science.aac5894

REPORTS

SOFT ROBOTICS

A 3D-printed, functionally graded soft robot powered by combustion

Nicholas W. Bartlett,^{1,2*} Michael T. Tolley,^{3†} Johannes T. B. Overvelde,¹ James C. Weaver,² Bobak Mosadegh,⁴ Katia Bertoldi,¹ George M. Whitesides,^{2,5} Robert J. Wood^{1,2}

Robotists have begun to design biologically inspired robots with soft or partially soft bodies, which have the potential to be more robust and adaptable, and safer for human interaction, than traditional rigid robots. However, key challenges in the design and manufacture of soft robots include the complex fabrication processes and the interfacing of soft and rigid components. We used multimaterial three-dimensional (3D) printing to manufacture a combustion-powered robot whose body transitions from a rigid core to a soft exterior. This stiffness gradient, spanning three orders of magnitude in modulus, enables reliable interfacing between rigid driving components (controller, battery, etc.) and the primarily soft body, and also enhances performance. Powered by the combustion of butane and oxygen, this robot is able to perform untethered jumping.

Robots are typically composed of rigid components to promote high precision and controllability. Frequently constructed from hard metals such as aluminum and steel, these robots require large machining equipment and an intricate assembly process. In contrast, recent work has explored the possibility of creating soft-bodied robots (1–6) inspired by invertebrates such as cephalopods (7–9) and insect larvae (10), as well as vertebrates, including snakes (11) and fish (12). The use of compliant materials facilitates the development of biologically inspired robotic systems (13) that

are more adaptable (14), safer (15, 16), and more resilient (17) than their fully rigid counterparts.

The design and fabrication of soft robotic systems, however, present significant engineering challenges (18, 19). The bodies of soft robots are typically fabricated in custom-designed molds and require multiple assembly steps (20) or lost-wax techniques (21) to embed actuation. The molds used to create these soft robots are complex and time-consuming to make, especially for prototype designs that are fabricated in small numbers and are constantly evolving. Additionally, some applications (such as ones

requiring untethered robots) require rigid components to power and control the soft body (11, 12, 17) or to perform specific tasks. The interfaces between these rigid components and the soft body of the robot are points of recurring failure.

In nature, many animals employ stiffness gradients to join rigid materials and soft structures while minimizing stress concentrations that could lead to failures at rigid/soft interfaces (22, 23). One of the reasons biological systems often outperform engineered systems is that in nature, which employs self-organization for fabrication, added structural complexity comes at a minimal cost. Emerging digital fabrication technologies (such as 3D printing) are beginning to allow designers to move toward this level of structural complexity, albeit at a larger scale and with fewer materials. These technologies can be used to manufacture geometrically intricate designs as efficiently as simple designs with an equivalent amount of material.

¹School of Engineering and Applied Sciences, Harvard University, Cambridge, MA 02138, USA. ²Wyss Institute for Biologically Inspired Engineering, Harvard University, Cambridge, MA 02138, USA. ³Department of Mechanical and Aerospace Engineering, University of California, San Diego, La Jolla, CA 92093, USA. ⁴Dalio Institute of Cardiovascular Imaging, Department of Radiology, New York-Presbyterian Hospital and Weill Cornell Medical College, New York, NY 10021, USA. ⁵Department of Chemistry and Chemical Biology, Harvard University, Cambridge, MA 02138, USA.

*Corresponding author. E-mail: nbartlett@seas.harvard.edu

†These authors contributed equally to this work.

We used a multimaterial 3D printer (Connex500, Stratasys) to directly print the functional body of a robot that employs soft material components for actuation, obviating the need for complex molding techniques or assembly (24). The robot body is composed primarily of two nested hemispheroids. The flexible bottom hemispheroid features a small depression that provides an initial volume into which oxygen and butane are injected. Ignition of the gases causes a volumetric expansion (25, 26), launching the robot into the air (Fig. 1, A and B). The top hemispheroid has a modulus of elasticity that ranges over three orders of magnitude (from approximately 1 MPa to 1 GPa) through a stepwise gradient of nine different layers, creating a structure that transitions from highly flexible (rubber-like) to fully rigid (thermoplastic-like). In addition to providing a mechanical interface for the rigid control components, the rigid portion of the top hemispheroid also prevents undesired expansion locally and focuses the energy of combustion into the ground, enhancing the jumping efficiency. Pneumatic legs, which use a nested hemi-ellipsoid design similar to that of the main body, surround the central explosive actuator and are used to tilt the body before a jump, controlling the direction of locomotion. This separation of power and control actuators simplifies actuation and gives greater control over direction.

In order to simplify prototyping, we chose a modular design with a rigid core module containing the control components (which are ex-

pensive and change infrequently during design iteration of the body), connected through a pre-defined interface to the body of the robot (Fig. 1C). This modularity enables efficient iteration of the robot body design, as well as rapid replacement in the case of destructive testing. The core module contains a custom circuit board, high-voltage power source, battery, miniature air compressor, butane fuel cell, bank of six solenoid valves, oxygen cartridge, pressure regulator, and an internal network of channels to facilitate interfacing between the components as necessary (fig. S1, A and B). The core module is mechanically attached to the rigid portion of the body with a layer of high-strength mushroom-head fasteners. Otherwise, it interfaces with the body only through four tubes (three pneumatic tubes for the legs and one tube for fuel delivery to the combustion chamber) and two wires (which produce the spark in the combustion chamber).

Characterization of nine 3D-printed materials with a set of mechanical tests informed the design of the 3D-printed rigid/soft robot. We performed qualitative twisting experiments to gain an intuitive understanding of the response of the various materials (Fig. 2A). Mechanical testing on a universal testing machine (Instron 5544, Instron) yielded quantitative values of material properties (supplementary text). This information was used to simulate the operation of the robot using finite element analysis (FEA) software, which allowed us to compare the relative efficiency of jumping robots with different

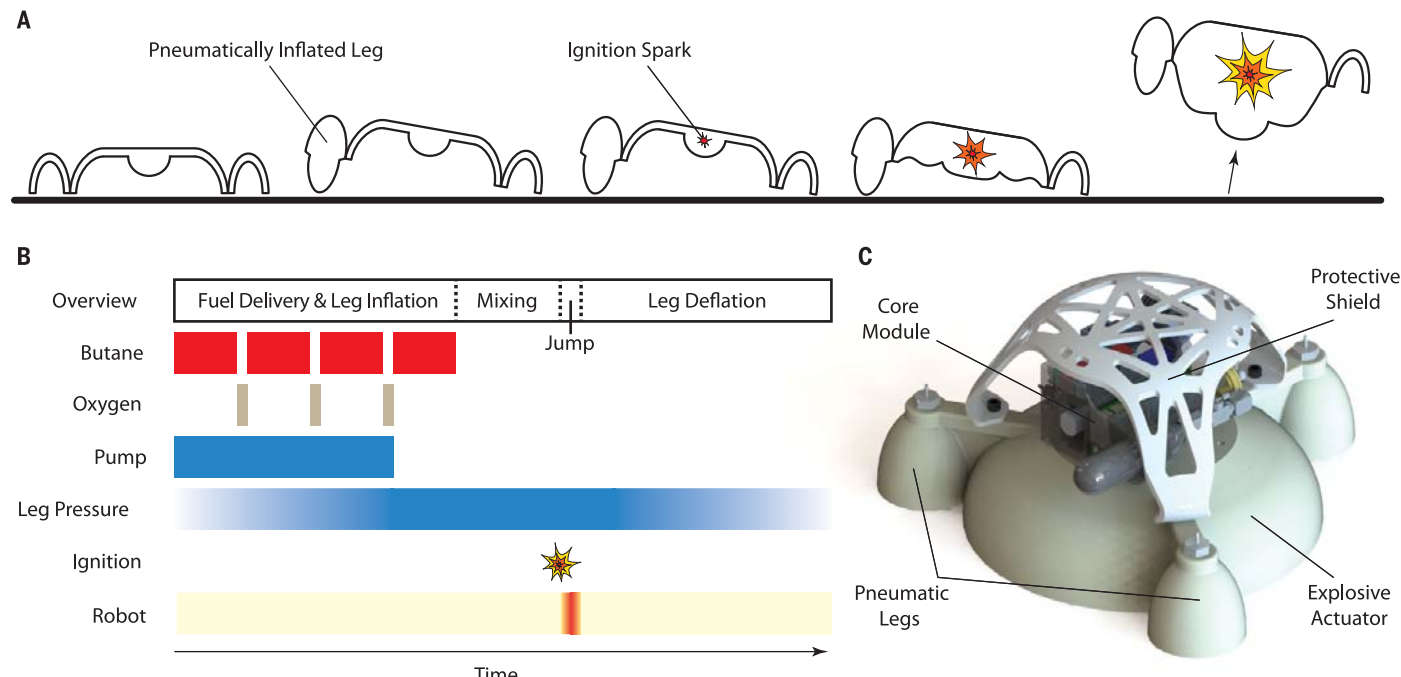


Fig. 1. Robot design and principle of operation. (A) To initiate a jump, the robot inflates a subset of its legs to tilt the body in the intended jump direction. Upon combustion, the bottom hemispheroid balloons out, pushing against the ground and propelling the robot into the air. (B) The ignition sequence consists of fuel delivery, mixing, and sparking. Butane and oxygen are alternately delivered to the combustion chamber (to promote mixing). After a short delay to

promote additional mixing of the fuels, the gaseous mixture is ignited, resulting in combustion. Leg inflation occurs concurrently with fuel delivery, and leg deflation begins shortly after landing. (C) Computer-aided design model of the entire robot, consisting of the main explosive actuator surrounded by three pneumatic legs. A rigid core module that contains power and control components sits atop the main body, protected by a semisoft shield.

material distributions. Further simulations allowed us to examine the differences in stress concentrations as a function of material distribution (fig. S2). The results from these studies revealed that, when compared to an abrupt material transition, the incorporation of a graded interface could achieve a 30% reduction in maximum stress upon tensile loading, reaching a value comparable to the maximum stress observed in a soft, single-material model. Although a perfectly smooth gradient from rigid to flexible would have been ideal, the capability

of the fabrication technique was limited to a stepwise gradient of at most nine materials. The actuation strategy necessitated a flexible bottom hemispheroid, whereas the off-the-shelf control components required a rigid housing; however, the stiffness distribution of the top hemispheroid was unconstrained. Thus, to determine how the material properties of the top hemispheroid would affect jumping, we simulated three cases: (i) a flexible top with a small rigid portion to mount control hardware, (ii) a top featuring a stiffness gradient from fully

flexible to fully rigid, and (iii) a fully rigid top (Fig. 2B and movie S1). Simulations showed that the flexible top was inefficient at directing the energy of combustion into the ground and propelling the robot, suggesting weak jump performance. As expected, the simulated rigid top robot produced the highest ground reaction force, whereas the gradient top robot exhibited a performance between the two extremes.

We carried out additional simulations to investigate the behavior of the three designs during the impact of landing (Fig. 2C and movie S1).

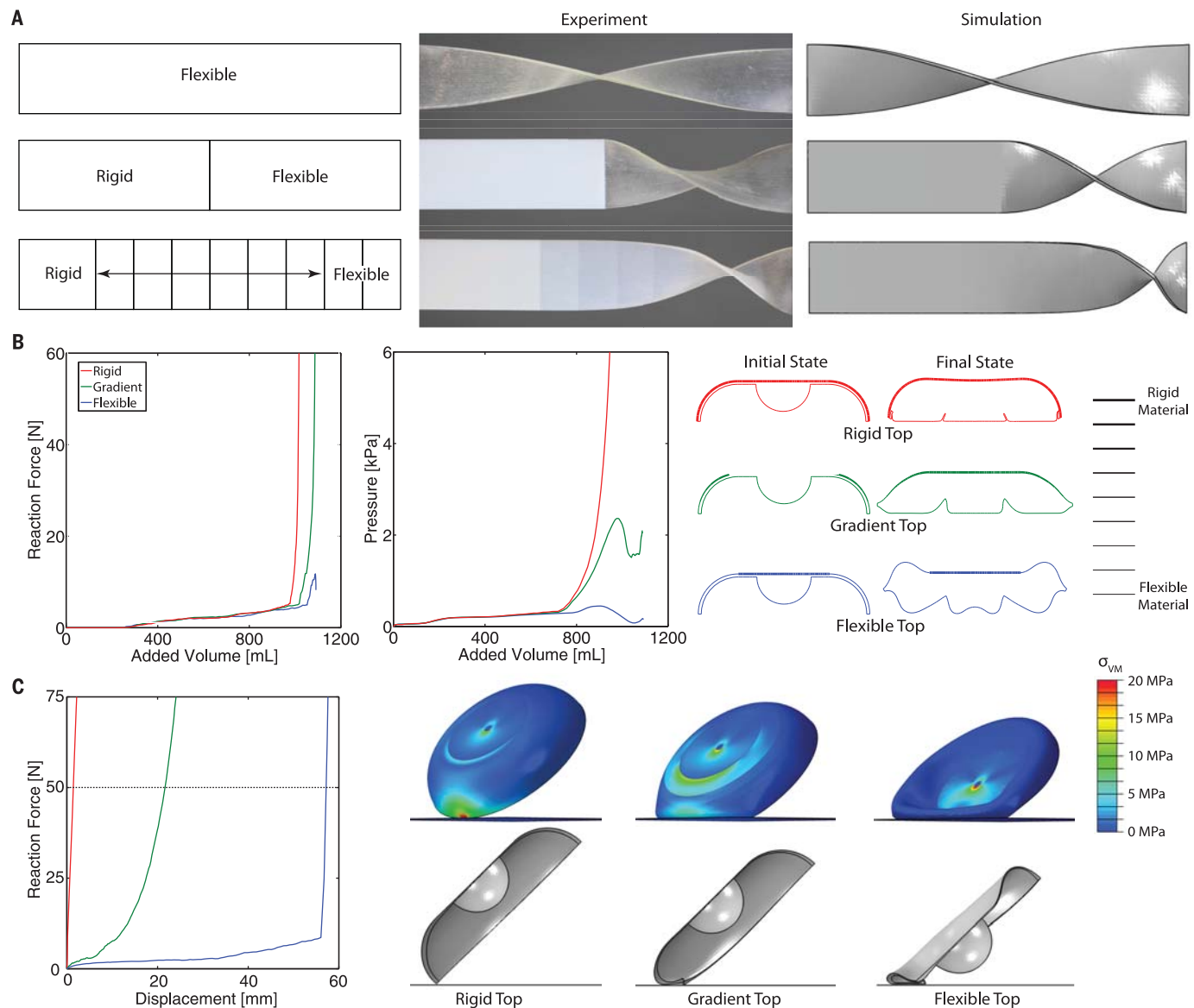


Fig. 2. Material tests and simulation results. (A) Qualitative twisting analysis comparing 3D-printed beams that are fully flexible, half rigid and half flexible, or transition gradually from rigid to flexible. These tests were performed to gain an understanding of how these materials respond, as well as to validate the numerical values of the material properties used in simulation. (Left) Material distribution of the beams. (Middle) Beams under torsion. (Right) Simulation of beams under torsion. (B) Jumping simulation. (Left) Ground reaction force experienced by the three robots upon striking a solid plane under simulated conditions representative of actual testing conditions. (Middle) Pressure evolution inside the robot body as internal gases expand. (Right) Deformation state of

rigid top, gradient top, and flexible top robot bodies at the initial state and the point of maximum simulated gas expansion. Line thicknesses indicate material stiffness. (C) Impact simulation. In the simulation, the robot strikes the ground at 45°. This angle was chosen as a particularly extreme loading condition and because it correlated with observations from jumping experiments. (Left) Reaction forces experienced by the three robots upon striking a solid plane under simulated conditions representative of actual testing conditions. (Right) FEA results of rigid top, gradient top, and flexible top robots, compared at 50 N.

The results indicate that the rigid top robot experiences a given reaction force (50 N) at a much smaller deformation than either the gradient or flexible top robots. Immediately upon impact, the rigid top robot experiences an abrupt increase in force, whereas the gradient top robot experiences a more moderate increase. The flexible top robot sees almost no increase, until the small rigid portion strikes the ground, initiating a rapid increase akin to that of the rigid top robot. Integrating the force-displacement curves (up to 50 N), we find that the rigid and flexible top robots only absorb 13 and 73% (respectively) of the impact energy that the gradient top robot absorbs. The increased energy absorbed by the gradient top robot during impact suggests that it will be most successful at distributing the impulse over a longer duration, therefore reducing peak stresses and providing the least violent landing.

By 3D-printing different test cases, we experimentally verified these simulation results. A jumping robot with a completely rigid top was able to jump 1.12 m untethered using 40 ml of butane and 120 ml of oxygen. Identical testing conditions on a gradient top robot produced a jump of 0.25 m. A flexible top robot was deemed impractical to print because of the predictions from FEA. As predicted by the simulations, the gra-

dient top robot was less efficient at jumping. However, the gradient top robot was better able to withstand the impact of landing (Fig. 3A and movie S2). In one test, the body of the rigid top robot shattered upon landing, surviving a total of just five jumps; the gradient top robot survived more than twice that number of jumps and remained operational. Other nearly identical gradient top robots survived over 100 jumps (in 81% of these tests, we removed the core module from the body and delivered the combustion products and ignition sparks through a tether to simplify testing, reducing the system mass to about 50% that of the untethered system). To provide a direct comparison in landing behavior, the gradient top robot was additionally dropped from the maximum height achieved by the rigid top robot and successfully survived 35 falls (supplementary text). The stiffness gradient provides the necessary rigidity to transfer the impulse of combustion to generate effective jumping, and the compliance of the base absorbs and dissipates the energy of the landing impact. By trading the jumping efficiency of the rigid robot for an improved ability to survive landings, the gradient top robot demonstrated a greater overall robustness.

Further testing on the gradient top robot showed high resilience and good performance (Fig. 3B and movie S2). This robot autonomously jumped

up to 0.76 m (six body heights) high and demonstrated directional jumping of up to 0.15 m (0.5 body lengths, 20% of jump height) laterally per jump (Fig. 3C and movie S2). Unlike previous combustion-powered soft jumpers that were either tethered (25) or achieved only a few untethered jumps due to inconsistent connection of electrical and mechanical components at the interface of the rigid and soft components (26), this design allowed for many successful jumps with a single soft robot (21 untethered jumps and 89 tethered jumps). Another jumper design has also shown the ability to perform multiple jumps, can operate on uneven terrain, and can even recover from landing in any orientation (27), although at the sacrifice of directional control. In our system, the high energy density of the fuels theoretically allows onboard storage of sufficient fuel for 32 consecutive jumps (supplementary text). The bodies were extremely robust, surviving dozens of jumps before they became unusable. The monolithic design has no sliding parts or traditional joints that can be fouled or obstructed by debris or rough terrain, and the nested design requires minimal deformation for actuation. As with previous jumping soft robots powered by combustion (25–27), and untethered systems exposed to direct flames (17), we did not observe significant damage to the soft (or rigid) body materials due to the brief

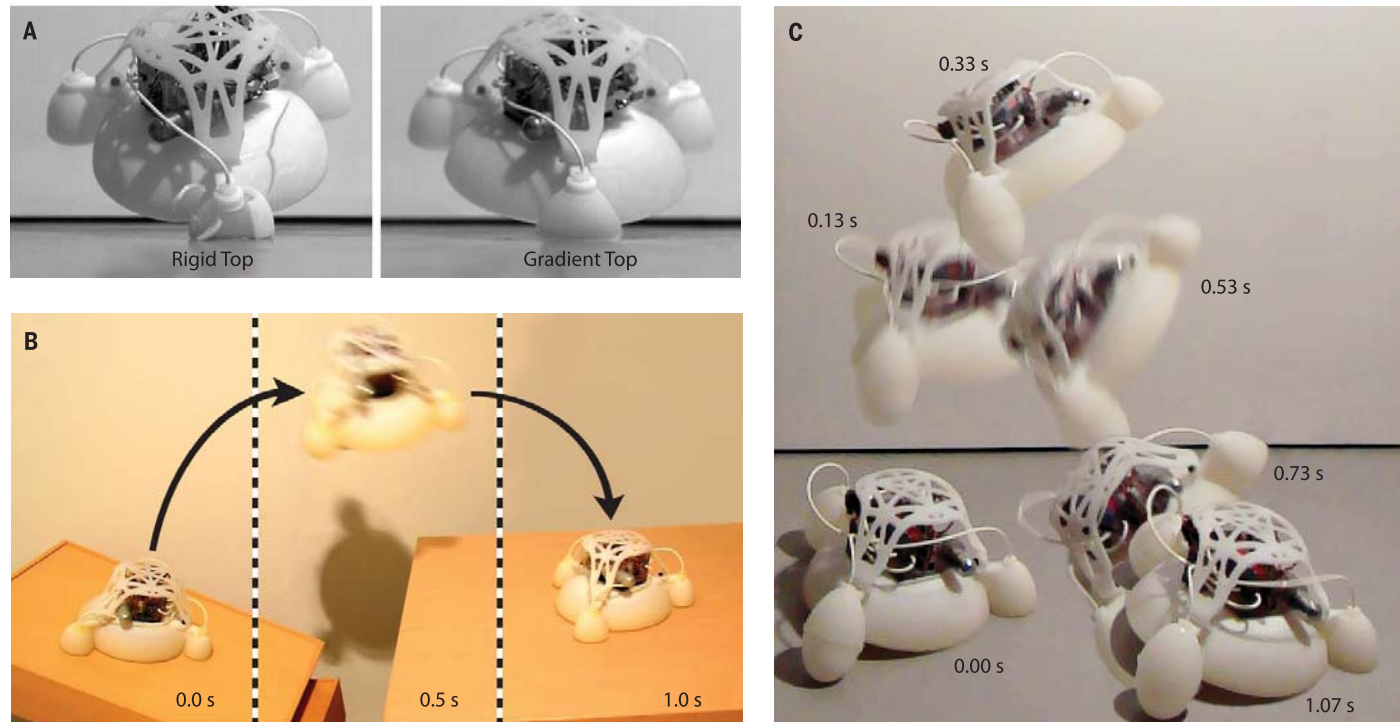


Fig. 3. Experimental testing results. (A) Frames shortly after the moment of ground contact from movie S2 (Impact Comparison). Identical testing conditions were used to analyze the difference in landing between a robot with a rigid top and one with a gradient top. Because the rigid top robot jumped higher under combustion-powered testing, the gradient top robot was dropped from the maximum height achieved by the rigid top robot for a direct comparison. (Left) The rigid top robot fractures upon impact. (Right) The gradient top robot is able to absorb the impact and survive the fall. (B) Frames from movie S2 (Jump onto Table) at various times. The robot performs a targeted jump off of an angled surface onto a table. (Left) As the robot prepares for the jump, oxygen and butane are delivered into the combustion chamber. (Middle) Upon ignition of the fuel, the robot is propelled into the air. (Right) After jumping across a gap, the robot lands on a table. (C) Frames from movie S2 (Directional Jump) at various times during a directional jump. The robot pitches backward during the jump, providing a soft landing on the inflated legs. Upon impact with the ground, the robot pitches forward and returns to its pre-jump stance.

(Jump onto Table) at various times. The robot performs a targeted jump off of an angled surface onto a table. (Left) As the robot prepares for the jump, oxygen and butane are delivered into the combustion chamber. (Middle) Upon ignition of the fuel, the robot is propelled into the air. (Right) After jumping across a gap, the robot lands on a table. (C) Frames from movie S2 (Directional Jump) at various times during a directional jump. The robot pitches backward during the jump, providing a soft landing on the inflated legs. Upon impact with the ground, the robot pitches forward and returns to its pre-jump stance.

exposure to elevated combustion temperatures and flames.

The fabrication of soft robots using multi-material 3D printing has numerous advantages over traditional molding techniques. This strategy promotes high-throughput prototyping by enabling rapid design iteration with no additional cost for increased morphological complexity. By allowing designers greater freedom, 3D printing also facilitates the implementation of good robotic design principles, such as modularity and the separation of power and control actuators. Beyond soft robotics specifically, the ability to print a single structure composed of multiple materials enables investigation into mechanically complex designs, without the drawbacks of complicated assembly or inconsistent manufacturing repeatability. One such design is a modulus gradient that eases the transition from soft to rigid components through stress reduction at the interface of materials mismatched in compliance. Although the materials available to this fabrication strategy are currently limited and perhaps best suited to the fabrication of prototype devices, future development of materials compatible with 3D printing will only enhance the relevance of this approach.

REFERENCES AND NOTES

- D. Rus, M. T. Tolley, *Nature* **521**, 467–475 (2015).
- D. Trivedi, C. D. Rahn, W. M. Kier, I. D. Walker, *Appl. Bionics Biomech.* **5**, 99–117 (2008).
- R. Pfeifer, M. Lungarella, F. Iida, *Commun. ACM* **55**, 76 (2012).
- S. Kim, C. Laschi, B. Trimmer, *Trends Biotechnol.* **31**, 287–294 (2013).
- C. Majidi, *Soft Robotics* **1**, 5–11 (2014).
- C. Laschi, M. Cianchetti, *Front. Bioeng. Biotechnol.* **2**, 1–5 (2014).
- W. McMahan et al., in *Proceedings of the 2006 IEEE International Conference on Robotics and Automation*, 15 to 18 May 2006, Orlando, FL, pp. 2336–2341.
- R. F. Shepherd et al., *Proc. Natl. Acad. Sci. U.S.A.* **108**, 20400–20403 (2011).
- C. Laschi et al., *Adv. Robot.* **26**, 709–727 (2012).
- H.-T. Lin, G. G. Leisk, B. Trimmer, *Bioinspir. Biomim.* **6**, 026007 (2011).
- C. D. Onal, D. Rus, *Bioinspir. Biomim.* **8**, 026003 (2013).
- A. D. Marchese, C. D. Onal, D. Rus, *Soft Robotics* **1**, 75–87 (2014).
- R. Pfeifer, M. Lungarella, F. Iida, *Science* **318**, 1088–1093 (2007).
- K. Suzumori, S. Iikura, H. Tanaka, *Control Syst. IEEE* **12**, 21–27 (1992).
- Y.-L. Park et al., *Bioinspir. Biomim.* **9**, 016007 (2014).
- P. Polygerinos, Z. Wang, K. C. Galloway, R. J. Wood, C. J. Walsh, *Robot. Auton. Syst.*; available at www.sciencedirect.com/science/article/pii/S0921889014001729.
- M. T. Tolley et al., *Soft Robotics* **1**, 213–223 (2014).
- H. Lipson, *Soft Robotics* **1**, 21–27 (2014).
- K.-J. Cho et al., *Int. J. Precision Eng. Manuf.* **10**, 171–181 (2009).
- F. Ilievski, A. D. Mazzeo, R. F. Shepherd, X. Chen, G. M. Whitesides, *Angew. Chem.* **123**, 1930–1935 (2011).
- E. Steltz, A. Mozeika, N. Rodenberg, E. Brown, H. M. Jaeger, in *Proceedings of the 2009 IEEE/RSJ International Conference on Intelligent Robots and Systems*, 10 to 15 October 2009, St. Louis, MO, pp. 5672–5677.
- T. J. Roberts, E. Azizi, *J. Exp. Biol.* **214**, 353–361 (2011).
- A. Miserez, T. Schneberk, C. Sun, F. W. Zok, J. H. Waite, *Science* **319**, 1816–1819 (2008).
- Materials and methods are available as supplementary materials on *Science Online*.
- R. F. Shepherd et al., *Angew. Chem.* **125**, 2964–2968 (2013).
- M. T. Tolley et al., in *Proceedings of the 2014 IEEE/RSJ International Conference on Intelligent Robots and Systems*, 14 to 18 September 2014, Chicago, IL, pp. 561–566.
- M. Loepfe, C. M. Schumacher, U. B. Lustenberger, W. J. Stark, *Soft Robotics* **2**, 33–41 (2015).

ACKNOWLEDGMENTS

This material is based on work supported by NSF under award number DMR-1420570; the Wyss Institute for Biologically Inspired Research; and an Army Research Office, National Defense Science and Engineering Graduate (NDSEG) fellowship. Any opinions,

findings, conclusions, or recommendations expressed in this material are those of the authors and do not necessarily reflect those of the funding organizations.

SUPPLEMENTARY MATERIALS

www.sciencemag.org/content/349/6244/161/suppl/DC1

Materials and Methods

Supplementary Text

Figs. S1 and S2

Table S1

References (28, 29)

Movies S1 and S2

27 February 2015; accepted 11 June 2015

10.1126/science.aab0129

APPLIED PHYSICS

Mid-infrared plasmonic biosensing with graphene

Daniel Rodrigo,¹ Odeta Limaj,¹ Davide Janner,² Dordaneh Etezadi,¹ F. Javier García de Abajo,^{2,3} Valerio Pruneri,^{2,3} Hatice Altug^{1*}

Infrared spectroscopy is the technique of choice for chemical identification of biomolecules through their vibrational fingerprints. However, infrared light interacts poorly with nanometric-size molecules. We exploit the unique electro-optical properties of graphene to demonstrate a high-sensitivity tunable plasmonic biosensor for chemically specific label-free detection of protein monolayers. The plasmon resonance of nanostructured graphene is dynamically tuned to selectively probe the protein at different frequencies and extract its complex refractive index. Additionally, the extreme spatial light confinement in graphene—up to two orders of magnitude higher than in metals—produces an unprecedentedly high overlap with nanometric biomolecules, enabling superior sensitivity in the detection of their refractive index and vibrational fingerprints. The combination of tunable spectral selectivity and enhanced sensitivity of graphene opens exciting prospects for biosensing.

Graphene has the potential to reshape the landscape of photonics and optoelectronics owing to its exceptional optical and electrical properties (1–3). In particular, its infrared (IR) response is characterized by long-lived collective electron oscillations (plasmons) that can be dynamically tuned by electrostatic gating, in contrast to conventional plasmonic materials such as noble metals (4–10). Furthermore, the electromagnetic fields of graphene IR plasmons display unprecedented spatial confinement, making them extremely attractive for enhanced light-matter interactions and integrated mid-IR photonics (11–14). Specifically, biosensing is an area in which graphene tunability and IR light localization offer great opportunities.

The mid-IR range is particularly well suited for biosensing, as it encompasses the molecular vibrations that uniquely identify the biochemical building blocks of life, such as proteins, lipids, and DNA (15). IR absorption spectroscopy is a powerful technique that provides exquisite bio-

chemical information in a nondestructive label-free fashion by accessing these vibrational fingerprints. Nevertheless, vibrational absorption signals are prohibitively weak because of the large mismatch between mid-IR wavelengths (2 to 6 μm) and biomolecular dimensions ($<10 \text{ nm}$). To overcome this limitation, high sensitivity can be achieved by exploiting the strong optical near fields in the vicinity of resonant metallic nanostructures (16–18); however, this comes at the expense of a reduced spectral bandwidth and is ultimately limited by the relatively poor field confinement of metals in the mid-IR (19).

Here, we report a graphene-based tunable mid-IR biosensor and demonstrate its potential for quantitative protein detection and chemical-specific molecular identification. Our device (Fig. 1A) consists of a graphene layer synthesized by chemical vapor deposition and transferred to a 280-nm-thick native silica oxide of a silicon substrate. Graphene nanoribbon arrays (width $W = 20$ to 60 nm and period $P \approx 2W$) are then patterned using electron beam lithography and oxygen plasma etching (20). A scanning electron microscope image and an atomic force microscope profile for typical samples are shown in Fig. 1, B and C. We apply an electrostatic field across the SiO_2 layer through a bias voltage (V_g)

¹Institute of BioEngineering, École Polytechnique Fédérale de Lausanne, CH-1015 Lausanne, Switzerland. ²Institut de Ciències Fotòniques, Mediterranean Technology Park, 08860 Castelldefels (Barcelona), Spain. ³Institut Català de Recerca i Estudis Avançats, 08010 Barcelona, Spain.

*Corresponding author. E-mail: hatice.altug@epfl.ch

This copy is for your personal, non-commercial use only.

If you wish to distribute this article to others, you can order high-quality copies for your colleagues, clients, or customers by [clicking here](#).

Permission to republish or repurpose articles or portions of articles can be obtained by following the guidelines [here](#).

The following resources related to this article are available online at www.sciencemag.org (this information is current as of July 9, 2015):

Updated information and services, including high-resolution figures, can be found in the online version of this article at:

<http://www.sciencemag.org/content/349/6244/161.full.html>

Supporting Online Material can be found at:

<http://www.sciencemag.org/content/suppl/2015/07/08/349.6244.161.DC1.html>

This article cites 23 articles, 4 of which can be accessed free:

<http://www.sciencemag.org/content/349/6244/161.full.html#ref-list-1>

This article appears in the following subject collections:

Engineering

<http://www.sciencemag.org/cgi/collection/engineering>



www.sciencemag.org/content/349/6244/161/suppl/DC1

Supplementary Materials for

A 3D-printed, functionally graded soft robot powered by combustion

Nicholas W. Bartlett,* Michael T. Tolley, Johannes T. B. Overvelde, James C. Weaver,
Bobak Mosadegh, Katia Bertoldi, George M. Whitesides, Robert J. Wood

*Corresponding author. E-mail: nbartlett@seas.harvard.edu

Published 10 July 2015, *Science* **349**, 161 (2015)
DOI: 10.1126/science.aab0129

This PDF file includes:

Materials and Methods
Supplementary Text
Figs. S1 and S2
Table S1
Captions for Movies S1 and S2

Other Supplementary Materials for this manuscript include the following:
(available at www.sciencemag.org/content/349/6244/161/suppl/DC1)

Movies S1 and S2

Materials and Methods

The Stratasys website provided general information regarding the 3D printed material used in this project (specifically, the “PolyJet Materials Data Sheet” and the “Digital Materials Data Sheet”). Published data sheets indicate that the materials used in the robot ranged in hardness from Shore A 27 to Shore D 83. We performed additional analysis of the 3D printed material through different tests on a universal testing machine (Instron 5544, Instron). Cyclic testing indicated that at high rates of extension, significant hysteresis was present due to the viscoelastic properties of the 3D printed material. However, at rates below 0.03125 mm/s, all viscous effects were negligible and the material behaved elastically. Each of the nine different materials used in the stiffness gradient was tested in a standard tensile test (ASTM D 638, Type IV), performed at 0.03125 mm/s to eliminate any rate dependent behavior. From this test, we obtained values for the shear and Young’s moduli of each material, which were subsequently used in the simulations. The material properties can be found in Table S1.

We conducted extension tests on samples that featured either an abrupt transition from the softest to the most rigid material or a more gradual step-wise transition by incorporating materials of intermediate moduli. In fatigue tests in which we repeatedly stretched the samples to an extension of 5 mm (20% of the test section) at 0.03125 mm/s, the discrete samples failed after an average of 436 cycles, whereas the gradient samples lasted an order of magnitude longer (most samples were discontinued after 24 hours of testing, over 8640 cycles).

We designed the robots using SolidWorks, a 3D computer aided design (CAD) software, and printed them with a multimaterial 3D printer (Connex500, Stratasys Ltd.). The body was printed as a single piece. We cleared residual support material from the 3D printing process through a small excavation hole using a high pressure washer (Powerblast High Pressure Water Cleaner, Balco UK). After clearing all of the support material, we sealed the excavation hole by attaching a custom 3D printed cap to the body with cyanoacrylate adhesive (Loctite 416, Henkel AG & Company, KGaA).

In addition to the custom fabricated body, the robot consisted of a number of off-the-shelf components. These include a lithium polymer battery (E-flite 180 mAh 2S 7.4V 20C, Horizon Hobby Inc.), a mini-diaphragm pump (KPV-14A, Clark Solutions), six miniature pneumatic solenoid valves (X-Valve, Parker Hannifin Corp.), a butane fuel cell (RC-31, Master Appliance Corp.), and a pressure regulator (PRD-2N1-0-V, Beswick Engineering Co.). Oxygen was stored in a repurposed 16g CO₂ cartridge, outfitted with a piercing fitting (GCP-1038-3V, Beswick Engineering Co.) and ball valve (MBV-1010-303-V, Beswick Engineering Co.). The high voltage source was obtained from components of a continuous ignition gas lighter (57549 Olympian GM-3X Gas Match, Camco Manufacturing Inc.). The circuit board was custom designed with an Atmel ATmega168 microcontroller, and was programmed using the Arduino IDE.

The timing sequence on the solenoid valves determined how much butane and oxygen was delivered to the combustion chamber. After fixing the settings on both the pressure regulator (which was in-line with the oxygen cartridge) and the valve of the butane fuel cell, we determined flow rates of oxygen and butane by opening the respective valves for a predetermined amount of time and measuring the amount of gas delivered by bubbling into an inverted graduated cylinder. This procedure was repeated throughout the testing period to ensure consistency.

The first step in the testing procedure was refilling the butane fuel cell (if necessary) and refilling the oxygen cartridge. The oxygen cartridge was filled from a supply tank of oxygen regulated to 90 psi, and then sealed using the ball valve. It was then threaded into the regulator on the robot, keeping the ball valve closed until the initiation of a new test. Due to the rapid use of oxygen, five oxygen cartridges were filled and used during each testing cycle.

We explored the space of butane to oxygen ratios extensively during testing, and found a baseline mixture of 50 mL of oxygen and 24 mL of butane per jump to be the most consistent. The volume of the oxygen cartridges and the filling pressure limited the number of jumps on a single cartridge to two (or three if the amount of fuel delivered was reduced appropriately).

The circuit board was designed to run the same program each time the robot was turned on. Adjustments to the program required plugging the circuit board directly into a computer and opening the Arduino IDE.

Experiments were recorded using both a DSLR camera (D600, Nikon Inc.) and a high-speed camera (Phantom v710, Vision Research Inc.). The latter was run at 1000 or 2000 frames per second and operated using Phantom Camera Control (PCC) software. For Figures 3B and 3C, the multiple video frames were background subtracted and merged using Adobe Photoshop (Adobe Systems).

Non-linear finite element analysis was performed using the commercial package Abaqus/Explicit (v6.12) (Abaqus Unified FEA, Dassault Systemes). All materials were modeled using a Neo-Hookean material model (27), each with a specific initial shear modulus. The shear moduli were determined experimentally by performing uniaxial tension tests and fitting the stress-strain curves using a least squares approximation.

To qualitatively show the effect of using materials with different moduli within the same structure, we deformed three beams with a different material distribution by twisting them 180 degrees. These beams were modeled using approximately 10,000 tetrahedral elements (Abaqus element code C3D4), and quasi-static conditions were assured by using a relatively long simulation time, as well as a small damping factor (Fig. 2A).

We simulated the behavior upon pressurizing the internal cavity of the robot, neglecting the dynamic effects that occur in experiments when actuating the robot. Instead, we ensured quasi-static conditions to generate smoother results that enable a better comparison between the different designs of the top hemispheroid. We modeled the hemispheroid using the same shear moduli as used for the beams, but to reduce computation time we used approximately 50,000 triangular shell elements (Abaqus element code S3R), instead of using solid tetrahedral elements. In the simulations, we fully account for contact between all faces of the model. We inflated the internal cavity by using the surface-based fluid cavity capability in Abaqus, and monitored the pressure during inflation. To determine the force that was generated during inflation, we fixed the top center of the top hemispheroid (1 cm diameter) and measured the vertical reaction force during inflation.

To determine the forces generated during impact, we used the same conditions as those used in inflation. All dynamic effects were neglected; instead the robot was slowly forced into the ground by displacing the top center of the top hemispheroid (1 cm diameter) down towards the ground, while monitoring the reaction force in the upward direction.

Supplementary Text

At a high level, we acknowledge that the design space is large, and that there are many good designs to meet the requirements of a jumping robot powered by combustion. The robot presented by Loepfe et al. (26) provides an example of an alternative design to a similar problem. The roly-poly geometry enabled their robot to recover from landing in any orientation and to be ready for the next jump. Our system featured a geometry that, while unable to recover from certain landing orientations, was able to control jump direction. Incidentally, it is interesting to see that they independently settled on the power actuator design of an inflated membrane; however, instead of a bistable design, they rely on material strain for membrane deflection. While membrane deflection decreases the power available for jumping, it further aids the robot in returning to its initial jump-ready configuration, as there is just one stable state. The large design space resulted in two designs that differ based on differently prioritized performance requirements. The robot from Loepfe et al. showed consistent, repeatable operation even on rough terrain, while our system demonstrated directional control and good robustness.

We tested multiple robot bodies, as the body design evolved iteratively (which was enabled by the modular design). Early bodies failed upon combustion of the fuel because of stress concentrations from the use of screws to attach the core to the body. When the screws were replaced by mushroom-head fasteners, the main section of the body would only fail under oblique impacts on landing from tests using elevated fuel levels. A common mode of failure was also the tearing of the soft, bottom hemi-ellipsoidal portion of the legs due to repeated inflation/deflation cycles and the poor fatigue properties of the flexible 3D printed material.

In the tests in which we compared the impact behavior of the gradient top robot to the rigid top robot, we dropped the gradient robot, with all of the control components attached, from the maximum height achieved by the rigid top robot. The robot was dropped from numerous orientations to mimic the variability in landing. The gradient top robot survived a total of 35 falls. Unlike the rigid top robot, in which structural failure was catastrophic, the failure mode of the gradient top robot on the 36th fall was a cracking of one of the legs, which is easily repairable with a urethane adhesive.

In the baseline testing condition, 50 mL of oxygen was used for each jump. The oxygen cartridge had an internal volume of 20 mL and was pressurized to 90 psi, giving an initial volume of oxygen (at STP) of 122 mL. Thus, there should have been 22 mL left after the two jumps. Measurement of the remaining oxygen showed that 14.5 ± 4.2 mL (N=6) was left. The discrepancy (~7.5 mL) is likely due to inaccuracies in determining the exact valve timing and imperfections in the press fits of the tubing, valves, and connectors.

The supply pressure effect was certainly a factor, as the pressure of the oxygen cartridge changed significantly from the first jump to the second. We accounted for this fact by using different valve timing on the first and second jumps. The correct timing was determined experimentally by (1) filling an oxygen cartridge to standard experimental conditions, (2) opening the valve and noting the time required to deliver 50 mL oxygen, then closing the valve, and (3) reopening the valve a second time to deliver the same amount of oxygen, again noting the (new) time. We found that after filling to 90 psi, a standard 16g CO₂ cartridge would deliver 50 mL of oxygen in 1.95 seconds. The now lower pressure cartridge would deliver the same volume of oxygen (50 mL) in 1.50 seconds upon opening the valve a second time.

Fuel measurements were taken periodically over months of testing, and thus conditions (e.g. ambient temperature, humidity, etc.) varied. As discussed above, the flow rate of oxygen was variable, and so fuel delivery was determined by experimenting with valve timing. For an oxygen cartridge filled to 90 psi, opening the valve for 1.95 seconds delivered 56.3 ± 5.8 mL ($N = 15$). The second valve opening of 1.50 seconds delivered 47.5 ± 2.7 mL ($N = 6$). The flow rate of butane was notoriously variable, depending on how much liquid butane was in the container, the orientation of the container, and how forcefully it was press fit into the core module. After a procedure that produced somewhat reliable results was established, we determined a flow rate of 1.1 ± 0.4 mL/s ($N = 21$).

In tethered experiments on the gradient top robot (in which the control hardware was off-board and thus the robot was significantly lighter), the robot achieved its highest jump of 2.35 m using 50 mL of butane and 120 mL of oxygen. With a body mass of 478.6 g, this jump corresponds to an efficiency of 0.18% (+0.11%, -0.05%). The most efficient jump was a tethered test that reached 1.60 m using 24 mL of butane and 50 mL of oxygen, corresponding to an efficiency of 0.26% (+0.15%, -0.07%). For the untethered system, a robot with a total mass of 964.6 grams jumped 0.76 m using 24 mL of butane and 50 mL of oxygen, corresponding to an efficiency of 0.25% (+0.14%, -0.07%). The amounts of oxygen and butane used for the maximum height jump and most efficient jump did not correspond to calculated stoichiometric ratios. However, given that fuel delivery was quantified by valve timing, the exact amount of butane or oxygen delivered was unable to be precisely determined. In addition, we did not actively remove the preexisting air from the system, meaning that some amount of air was present in the combustion chamber in addition to the delivered amounts of oxygen and butane. Another source of error was the possibility that some of the butane was being absorbed into the walls of the combustion chamber.

Using smaller volumes of butane and oxygen, we were able to achieve multiple successive jumps in the tethered gradient top system. We demonstrated multiple jumps of differing heights (1.00 m jump followed by 0.30 m jump), as well as multiple jumps of roughly the same height (0.15 m and 0.15 m, also 0.50 m and 0.30 m).

As oxygen was the limiting fuel source, additional jumps could have been achieved by increasing the pressure of the stored oxygen. The pressure canister we used had an internal volume of 20 mL and is rated to contain pressures up to 6.2 MPa (900 psi). At this pressure, the canister could hold 1.62 g of oxygen, which is equivalent to 1.22 L at room temperature (20°C) and atmospheric pressure. This amount of oxygen is enough for 32 consecutive jumps. A full butane fuel cell holds 3.3 g of butane, or 1.38 L of gaseous butane at room temperature and atmospheric pressure, or enough for 57 jumps. Thus, oxygen was the limiting fuel. For safety reasons, we used oxygen pressurized to only 90 psi and replaced the oxygen supply after two jumps.

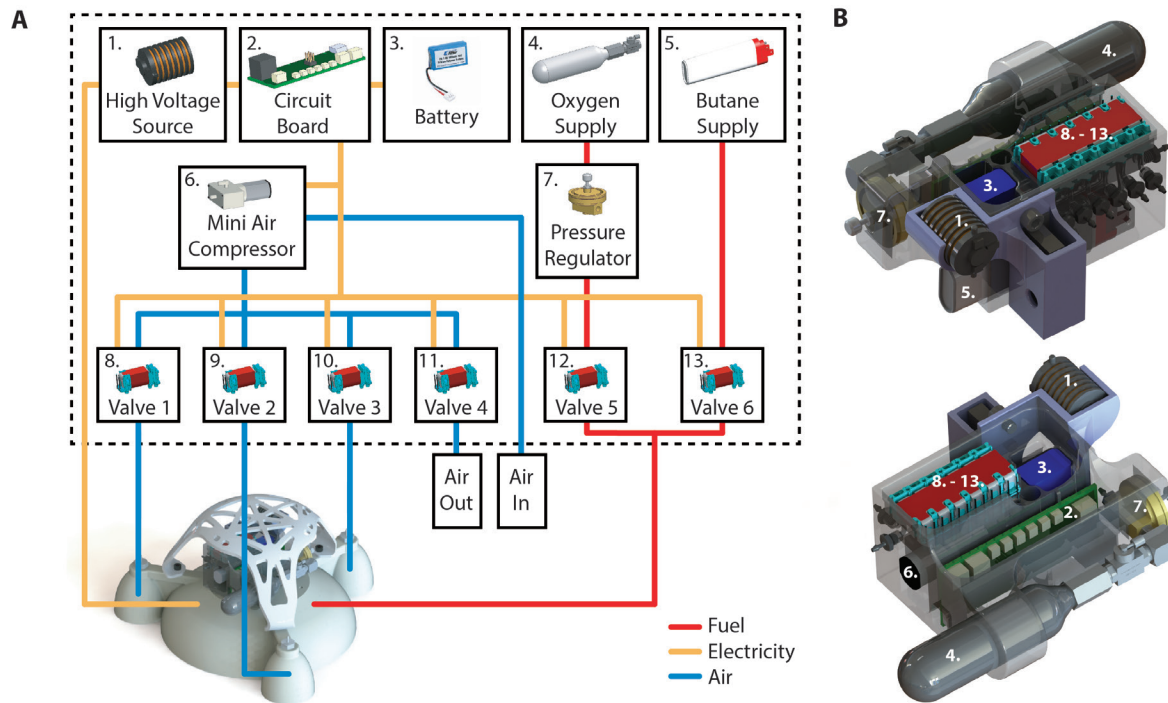


Fig. S1. Driving components and core module. (A) Functional dependencies of the control hardware. (B) CAD model of the core module with components from (A) labelled.

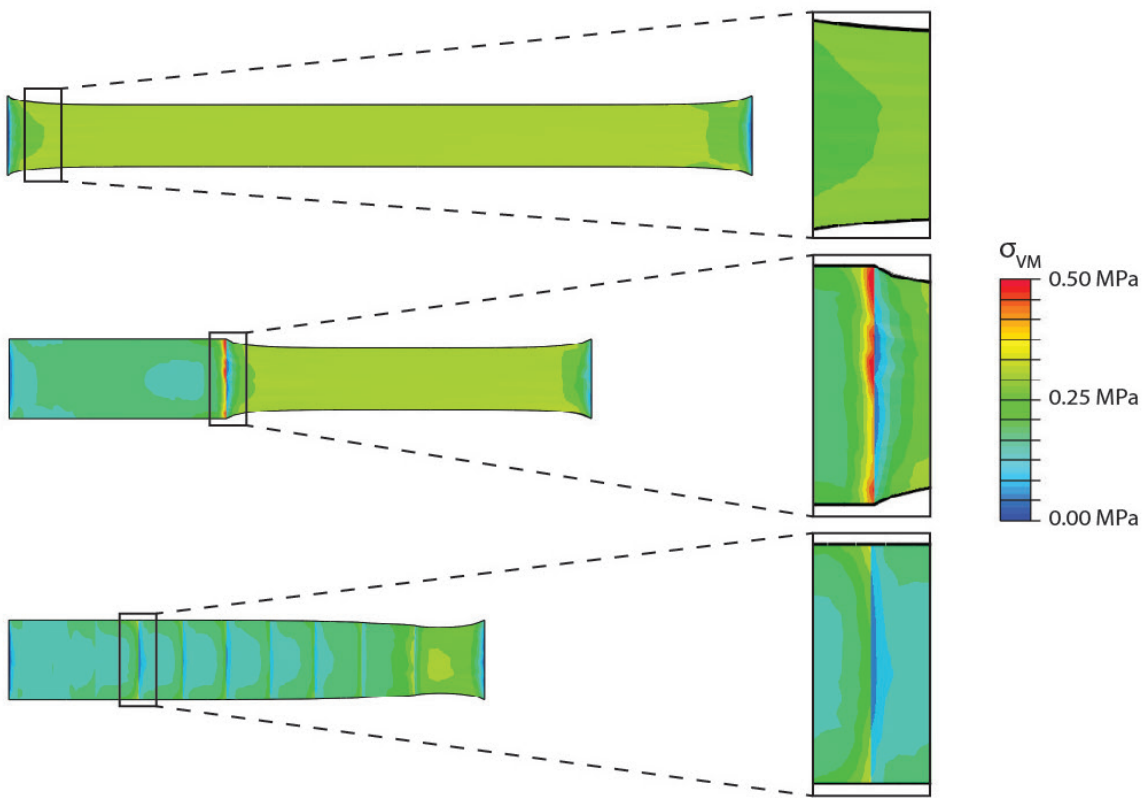


Fig. S2. Simulations of beams in tension. Simulations of beams in tension that are fully flexible (top), half rigid and half flexible (middle), and transition gradually from rigid to flexible (bottom). The maximum stresses in each of these beams are 0.35 MPa, 0.54 MPa, and 0.37 MPa, respectively. Compared to the half rigid and half flexible beam, the fully flexible and gradient beams experience maximum stresses of 64.8% and 68.5%, respectively. Simulations were done with (undeformed) beam dimensions of 25.4 mm x 152.4 mm x 1.0 mm. Enlarged images of the points of stress concentration are shown to the right of each beam. Additional motivation for the use of a gradient was derived from considerations of the effect of stress concentrations on interfacial failure in multi-material systems, a problem that is well established in the mechanics literature (28).

Material	Young's Modulus (MPa)
1	1012.5
2	802.90
3	58.462
4	52.641
5	15.309
6	6.767
7	2.698
8	1.166
9	0.439

Table S1. Young's moduli of the materials in the gradient. The materials used were digital combinations of commercial 3D printing materials offered by Stratasys, specifically VeroWhitePlus RGD835 (rigid) and TangoPlus FLX930 (flexible). Detailed information on these materials may be found on the Stratasys website (http://www.stratasys.com/~/media/Main/Secure/Material%20Specs%20MS/PolyJet-Material-Specs/Digital%20Materials_Datasheet-08-13.pdf).

Movie S1

This movie depicts the animated simulation results, as in Fig. 2. The first sequence shows the evolution of body shape for the rigid top, gradient top, and flexible top robots as the volume of the gas inside the body expands. The second sequence compares the impact behavior of the same three cases.

Movie S2

This movie presents the results of experimental testing, as in Fig. 3. The first sequence compares the impact behavior of the rigid top and gradient top robots. The second sequence depicts the robot performing a targeted jump off of an angled surface, and includes high-speed video of the takeoff. The final sequence shows the robot performing a directional jump on a flat surface.